Transitions and scaling in horizontal convection driven by different temperature profiles

Tzekih Tsai [a],[*], Wisam K. Hussam [a],[b], Martin P. King [c], Gregory J. Sheard [a]

[a] The Sheard Lab, Department of Mechanical and Aerospace Engineering, Monash University, VIC, 3800, Australia
[b] School of Engineering, Australian College of Kuwait, Safat, 13015, Kuwait
[c] Norce Norwegian Research Centre, and Bjerknes Centre for Climate Research, NO 5008, Bergen, Norway

ARTICLE INFO

ABSTRACT

Horizontal convection has been used as an idealised model of the ocean overturning circulation, where some non-uniform buoyancy forcing profile is imposed along a horizontal boundary. Several different driving temperature profiles have been chosen for past numerical and laboratory studies, likely for convenience, yet the effect of the shape of the chosen profile on the resulting horizontal convection flow remains unexplored. Here high order numerical simulation is used to investigate this problem. Time independent, periodic and chaotic regimes are identified as functions of Rayleigh number (Ra) and profile shape, with a step temperature profile being found to be more unstable than a linear temperature profile. Using a nonlinear Stuart–Landau analysis, the primary instability is consistently found to occur through a supercritical (non-hysteretic) bifurcation. This research highlights the importance of the horizontal buoyancy forcing profile in determining the thermal forcing required to produce instability in horizontal convection. In addition, Nusselt number scales to $Ra^{1/5}$ in the fully convective regime, with scaling exponents elevating beyond $Ra \approx 10^{10}$. This elevated scaling was more pronounced for the linear thermal boundary profile than for the step profile over the computed Rayleigh numbers range.

1. Introduction

Heat is transported through fluid media in a number of different ways which produces various physical phenomena as seen in natural systems as well as in engineering applications. One such process is through convection where heat and mass are transported both by molecular diffusion as well as advection of large-scale motion within the fluid. Thermally driven buoyancy flow is important in the fields of geophysical flows [1,2] as well as industrial applications [3]. The canonical Rayleigh–Bénard convection has been extensively studied (for reviews see Refs. [4–6]) since it was first examined by Bénard [7] experimentally and subsequently explained theoretically by Rayleigh [8]. In Rayleigh–Bénard convection, fluid motion is induced in a plane horizontal layer of fluid heated from below by destabilisation of the vertical thermal gradient. In contrast, this paper examines thermal convection where a horizontal thermal gradient along a single horizontal boundary invokes a natural convection flow; this class of convection is called horizontal convection [9].

Horizontal convection has been used as an idealised model to gain insight into the ocean overturning circulation [9–11], where the enclosure can be thought of as an idealisation of a meridional slice of an ocean basin, and the non-uniform heating (or temperature) imposed along one of the horizontal boundaries idealises the lateral variation in solar heating and surface temperature. Just as a thermohaline circulation sees warm surface waters advected from subtropical towards polar latitudes, where they cool and sink (forming "deep" and "bottom" waters Warren [12]), in horizontal convection fluid advects from a region of stable stratification to an unstable region where vertical transport away from the boundary takes place. Horizontal convection is often established in the laboratory via heating and cooling at the bottom boundary of an enclosure [10]; thus heating/cooling, upwelling/downwelling are interchanged with respect to the oceans. One of the striking features of large scale oceanic circulation is the formation of deep and bottom water from relatively small regions of ocean surface Stommel Bilgen and Yedder [13]. This bears some similarity to the narrow vertical plume region in horizontal convection, where the vertical transport of fluid away from the heated/cooled boundary takes place over a very small proportion of that boundary, while the return flow is diffusive, slow, and spread across a much larger proportion of the

---

* Corresponding author.
E-mail address: Tzekih.Tsai@monash.edu (T. Tsai).

Nomenclature

A	complex amplitude
c_p	specific heat capacity of the fluid
$\widehat{e}_y$	unit vector in the y-direction
E_k	kinetic energy of a Fourier wavenumber k
f_0	fundamental frequency
k	out-of-plane Fourier wavenumber
g	gravitational acceleration
h	height of fluid layer responsible for large-scale flow
H	enclosure height
L	enclosure width; characteristic length of thermal forcing for horizontal convection
l	Stuart–Landau model coefficient
n	temperature profile shape parameter
p	pressure
Pr	Prandtl number, $Pr = \nu/\kappa$, here $Pr = 6.14$ throughout
Ra	Rayleigh number based on imposed temperature difference across heated horizontal boundary
Ra_F	Rayleigh number based on imposed thermal flux across heated horizontal boundary
Ra_{cr}	critical Rayleigh number
Re	Reynold number

t	time
$\boldsymbol{u}$	velocity vector
x	Cartesian horizontal coordinate
y	Cartesian vertical coordinate
z	Cartesian transverse (out-of-plane) coordinate
α	fluid volumetric expansion coefficient
γ	real and non-negative amplitude of A
$\varepsilon, \varepsilon_u$	kinetic energy dissipation rate
ε_θ	thermal dissipation rate
η	Kolmogorov scale
η_b	Batchelor microscale
θ	fluid temperature
θ_0	fluid reference temperature
δ_θ	temperature difference imposed across horizontal boundary
κ	fluid thermal diffusivity
λ_u	kinetic boundary layer thickness
λ_θ	thermal boundary layer thickness
ν	fluid kinematic viscosity
ρ_0	fluid reference density
σ	linear growth rate
φ	phase angle
ω	angular oscillation frequency

boundary.

Numerous horizontal convection studies have employed different buoyancy forcing profiles, including linear temperature profiles [14,15] and combinations of fixed-temperature [16,17] and fixed heat flux [10] conditions along a horizontal boundary within a rectangular enclosure. In addition [18], studied convection heat transfer in an enclosure heated sinusoidally but it was heated on a vertical side wall with all other walls insulated. Khansila and Witayangkurn [19] performed a similar investigation in an enclosure filled with porous medium. More recently, Griffiths and Gayen [20] investigated a system forced by thermal variation in both horizontal directions, and found horizontal convection to share significant similarities to Rayleigh–Bénard convection. However, to date there has been no comprehensive study into the behaviour of horizontal convection with systematic variation of the imposed buoyancy forcing profile [21].

Despite the different driving temperature variations imposed throughout the literature, horizontal convection nevertheless tends to exhibit consistent behaviour with increased Rayleigh numbers: for any finite Rayleigh numbers, a natural convection circulation is invoked; at low Rayleigh numbers conduction dominates, no distinct boundary layers are observed, and the Nusselt number is Rayleigh-number-invariant; beyond a sufficient Rayleigh number convection dominates with distinct thermal and kinetic boundary layers developing adjacent to the thermal forcing boundary. In this convective regime, it is well-established that Rossby's $Nu \sim Ra^{1/5}$ scaling is produced. Evidence supporting Rossby's scalings at Rayleigh numbers sufficient to invoke the convective regime is plentiful. Numerical and laboratory experiments by Mullarney et al. [10] demonstrated a Nusselt number scaling against a thermal flux-based Rayleigh number $Nu \sim Ra_F^{1/6}$ equivalent to a $Ra^{1/5}$ scaling, while other numerical studies have directly demonstrated the $Nu \sim Ra^{1/5}$ scaling up to Rayleigh numbers $Ra = \mathcal{O}(10^9)$ [23,24] and $Ra = \mathcal{O}(10^7)$ [15]. Numerical simulations by Sheard and King [24] and Ilıcak and Vallis [25] each demonstrated a $Ra^{-1/5}$ scaling for forcing boundary layer thickness.

Numerically, horizontal convection has been shown to become unsteady beyond some critical Rayleigh number, capable of maintaining overturning circulation within an enclosure [17,23,26]. Sheard and King [24], who employed a linear thermal profile, detected an elevation

of the Nusselt number scaling exponent beyond $Ra^{1/5}$ for Rayleigh numbers $Ra > \mathcal{O}(10^{10})$. Higher scaling exponents are accommodated under the variational analysis of Siggers et al. [23] that identifies the upper bound as $Nu \sim Ra^{1/3}$ for horizontal convection. Gayen et al. [17] (who used a step change in temperature along the heated boundary) detected a brief elevation in scaling beyond $Ra^{1/5}$ before reversion to the original scaling at higher Rayleigh number. More recently, Shishkina et al. [27] adapted the scaling theory developed by Grossmann and Lohse [28] for Rayleigh–Bénard convection to a horizontal convection configuration where global averaged kinetic and thermal dissipation rates are decomposed into boundary layer and bulk contributions. Their theory captures Rossby's $Nu \sim Ra^{1/5}$ scaling [22] in regime I_l, characterised by the thermal boundary layer being thicker than the kinetic layer, and both thermal and kinetic dissipation being dominant in the boundary layers, and several regimes that predict a Nusselt number scaling going with $Ra^{1/4}$.

On the other hand, Griffiths and Gayen [20] investigated thermal forcing which varied in both horizontal directions coupled with a length scale smaller than the domain. Their results demonstrated available potential energy can be produced without necessary changing the total supply of potential energy, this production is a driver for convection in their setup. This was further investigated experimentally and numerically by Rosevear et al. [29]. They found that the normalised heat transfer scales as $Nu \sim Ra^{1/5}$ for shallow enclosures and scales as $Nu \sim Ra^{1/4}$ for deep enclosures. The 1/4 scaling regime was explained as a large scale motion within the interior and thermal diffusion through stabilised parts of the boundary layer. Hence recent years have seen an accumulation of evidence that the choice of thermal boundary conditions in horizontal convection may influence the scalings in the flow.

The aim of this study is to investigate the effect that different temperature profiles imposed on the thermal forcing boundary have on horizontal convection scaling and stability. This will shed more light on the robustness of Nusselt number scaling at high Rayleigh numbers as well as under different imposed temperature condition. In addition, Fourier analysis will be used to explain the nature of the unsteady flow at high Rayleigh numbers.

This paper is structured as follows: § 2 gives a detailed description of the numerical setup and mesh resolution study. This is followed in § 3 by

results and discussion, while conclusions are drawn in § 4.

2. Numerical setup

The system comprises a rectangular enclosure of width L and height H filled with fluid having reference density ρ_0, kinematic viscosity ν, thermal diffusivity κ and volumetric expansion coefficient α, as depicted in Fig. 1. The flow is driven by a non-uniform temperature profile applied along the bottom of the enclosure, with a temperature difference of $\delta\theta$ from the cold (left) to hot (right) end. Fluid temperature θ and pressure p are respectively expressed relative to a fixed reference temperature θ_0 taken at the mid-point of the bottom boundary, and an arbitrary reference pressure p_0. Throughout this study lengths, time t, velocity $\boldsymbol{u}$, pressure and temperature are respectively scaled by L, L^2/κ, κ/L, $\rho_0\kappa^2/L^2$ and $\delta\theta$. All quantities are expressed in their dimensionless form hereafter.

A family of temperature profiles for the bottom boundary is constructed based on a power function that smoothly varies between a step profile and a linear profile as an exponent n is varied over $0 \le n \le 1$. The expression for the temperature profile is

$$\theta_{\text{cold}} = -\frac{1}{2}\left|2x - 1\right|^n, \quad 0 \le x \le 0.5$$
$$\theta_{\text{hot}} = +\frac{1}{2}\left|2x - 1\right|^n, \quad 0.5 < x \le 1 \tag{1}$$

The temperature therefore varies over $-0.5 \le \theta|_{y=0} \le 0.5$ over the base as shown in Fig. 2, and when the system reaches thermal equilibrium there is no net heat transport across the forcing boundary. Simulations are initialised with an interior temperature $\theta|_{t=0} = 0$.

The side and top walls are thermally insulated (zero temperature gradient normal to the walls), and a no-slip condition is imposed on the velocity field on all walls. A Boussinesq approximation for fluid buoyancy is employed, whereby density differences in the fluid are neglected except through the gravity term in the momentum equation. Under this approximation the energy equation reduces to a scalar advection-diffusion equation for temperature which is evolved in conjunction with the velocity field. The fluid temperature is related linearly to the density via thermal expansion coefficient α. The Navier–Stokes equations governing a Boussinesq fluid may be written as

$$\frac{\partial \boldsymbol{u}}{\partial t} = -(\boldsymbol{u} \cdot \nabla)\boldsymbol{u} - \nabla p + Pr\,\nabla^2\boldsymbol{u} + Pr\,Ra\,\theta\widehat{e}_y, \tag{2}$$

$$\nabla \cdot \boldsymbol{u} = 0, \tag{3}$$

$$\frac{\partial \theta}{\partial t} = -(\boldsymbol{u} \cdot \nabla)\theta + \nabla^2\theta, \tag{4}$$

where $\widehat{e}_y$ is the unit vector in the y-direction. The horizontal Rayleigh number characterising the ratio of buoyancy to thermal and molecular dissipation is
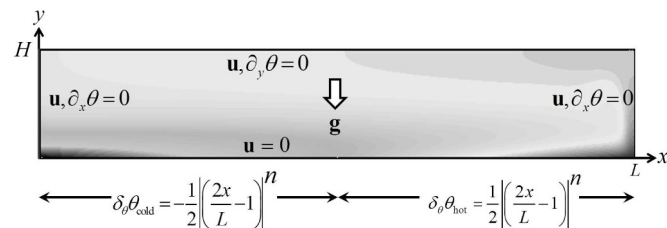

Fig. 1. A schematic representation of the computational domain under investigation with the prescribed boundary conditions along each of the boundary. The domain has an aspect ratio of $H/L = 0.16$, the same aspect ratio is used throughout this study. The equations used for the forcing temperature along the bottom boundary are expressed here in dimensional form.
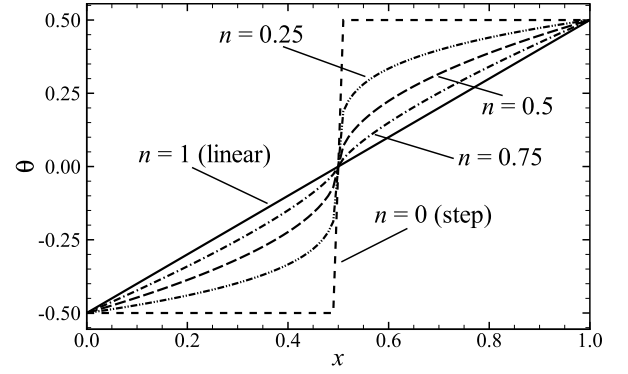

Fig. 2. Illustrating the shapes of the imposed temperature profile along the bottom forcing boundary of the computational domain. The temperature profile consists of a variation from a linear ($n = 1$) profile to a step profile ($n = 0$). The temperature and lengths are expressed in dimensionless form as described in § 2.

$$Ra = \frac{g\alpha\delta\theta L^3}{\nu\kappa}, \tag{5}$$

where g is the gravitational acceleration. The Prandtl number characterising the ratio of molecular to thermal diffusion in the fluid is

$$Pr = \nu/\kappa, \tag{6}$$

and throughout this study $Pr = 6.14$, which approximates water at laboratory conditions (at 25^oC). The Nusselt number characterising the ratio of convective to conductive heat transfer is

$$Nu = \frac{F_\theta L}{\rho_0 c_p \kappa \delta\theta}, \tag{7}$$

where heat flux

$$F_\theta = \kappa \rho_0 c_p \overline{\frac{\partial \theta}{\partial y}}, \tag{8}$$

c_p is the specific heat capacity of the fluid, and $\overline{\partial\theta/\partial y}$ is the averaged absolute vertical temperature gradient along the forcing boundary.

Rotation is known to have a significant effect on horizontal convection for rotation rates sufficient to reduce the Ekman layer to a thickness less than that of the horizontal convection boundary layers in a corresponding non-rotating system [9,21,30–32]. However, here rotation effects are deliberately neglected to isolate the fundamental effect of different temperature profiles on horizontal convection.

The system under consideration has a horizontal length L and a height H chosen to give an aspect ratio $H/L = 0.16$, as depicted in Fig. 1. This aspect ratio had been used in numerous studies including Mullarney et al. [10] and subsequent numerical simulations [17]. It has been shown [24] that the flow dynamics of horizontal convection are independent of aspect ratio at high Rayleigh numbers. At high Rayleigh numbers the thermal and kinetic boundary layers thicknesses are very much smaller than the enclosure height, $\delta_\theta, \delta_u \ll H$, thus the flow dynamics are independent of H. By comparison, this is far larger than the aspect ratio in the ocean where the horizontal length scale can be thousands of kilometres across with a vertical spatial scale of 1–5 km.

2.1. Mesh resolution study

The governing equations (2)–(4) are solved with an in-house solver featuring a high order nodal spectral element method for spatial discretisation and a third-order time integration scheme based on backward-differencing. This code had been validated in several studies

on planar and rotating horizontal convection flows [24,31].

For three-dimensional simulations, a Fourier expansion is used in the out-of-plane direction with a periodic boundary condition for simplicity and because sidewall effects are not being investigated in the current setup. An out-of-plane width of $0.04L$ is used, which is sufficient to capture several longitudinal rolls based on the prediction of linear stability analysis [33] and behaviour observed in recent simulations [17].

The computational mesh used to discretise the spectral element (x-y) plane in the current study consists of 12500 macro elements with clustering adjacent to all four walls, part of the macro mesh is shown in Fig. 3. In order to fully resolve small scale structures in thermal convection [34,35], showed that more grid points are needed within the thermal boundary layer as Rayleigh number increases. In this paper, a clustering factor is chosen to ensure sufficient grid points are used to resolve the thin thermal boundary layer along the bottom boundary as well as end wall plumes at high Rayleigh numbers. Based on Rossby's [22] laminar boundary layer scaling, the thermal boundary layer thickness scaled with $Ra^{-1/5}$. This would give an estimated thermal boundary layer thickness of $\approx 2.5 \times 10^{-3}$ for a given Rayleigh number of 10^{13}. The mesh has 6 spectral elements within this thin thermal boundary layer. Considering the polynomial order of 5 used for low Rayleigh numbers simulations and up to 7 for high Rayleigh numbers, this provides more than 30 quadrature points across the thermal layer. In addition to the thermal layer along the forcing boundary, thermal plumes are expected to travel along the right end wall into the interior; the mesh is carefully constructed in order to resolve plumes as they rise above the thermal layer as well as any thermal layer along the vertical end wall.

To determine an optimal element polynomial order to be used in the simulations, a resolution study is conducted for the mesh at $Ra = 5 \times 10^8$. The successive percentage error in the Nusselt number, $\mathcal{L}^2$ norm, and mean enclosure temperature are used to examine the solution convergence. The results are shown in Fig. 4. In terms of the Nusselt number, the error dropped below 10^{-6}% for polynomial orders ≥ 5. This error is close to 10^{-9}% with a polynomial degree of 8, which reflects the spectral convergence property of the spectral element method, and the quality of the mesh. Further evidence can be seen in the convergence of $\mathcal{L}^2$ norm and mean enclosure temperature, which are below 10^{-5}% for polynomial orders ≥ 5. The degrees of freedom trend plotted in the figure illustrates the increased computational cost needed to compute at higher polynomial orders. With this in mind, a polynomial order of 5 is chosen to compute at $Ra \leq 10^{11}$, which is progressively increased to 7 for higher Rayleigh number cases in order to capture the thinner thermal layer at these higher Rayleigh numbers.

In addition to the thermal boundary layer, at $Ra \geq 10^{10}$ the flow is increasingly unsteady, the overall kinetic energy production rate (the dissipation rate) and the viscosity will determine the smallest scales in the flow. The Kolmogorov length scale obtained from a dimensional
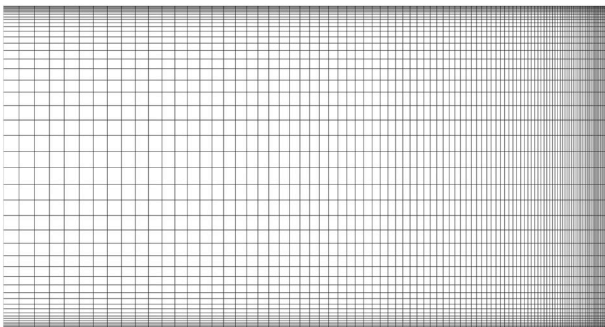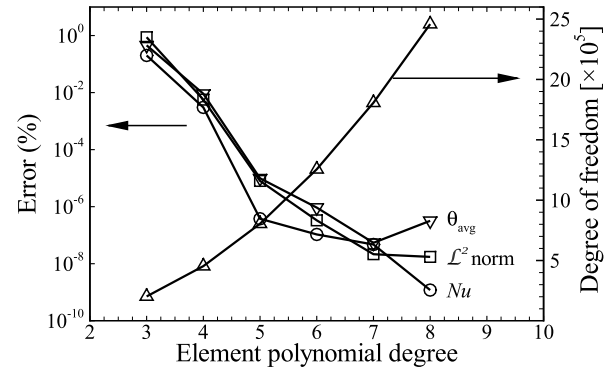

Fig. 4. Errors of the Nusselt number (Nu), averaged enclosure temperature (θ_{avg}) and the $\mathcal{L}^2$ norm plotted against the degree of polynomial order of the spectral elements used in the numerical simulation. This computation had $n = 1$, $Ra = 5 \times 10^8$ and $Pr = 6.14$. The total number of degree of freedom for the whole computational domain is included to highlight the increase in computation cost as the polynomial degree is increased.

analysis of the dissipation rate and viscosity is given by

$$\eta = \left(\frac{\nu^3}{\varepsilon} \right)^{1/4}. \tag{9}$$

The Kolmogorov scale must be resolved in order to fully capture small-scale features in the flow. In thermal convection at $Pr > 1$, the slower diffusion of temperature demands the resolution of the smaller Batchelor microscale, given by

$$\eta_b = \eta Pr^{-1/2}. \tag{10}$$

As in Ref. [28], local kinetic energy dissipation rate is given as

$$\varepsilon = \nu \left(\partial_i u_j(\boldsymbol{x}, t) \right)^2 \tag{11}$$

where here tensor notation has been employed for compactness. The local kinetic energy dissipation rate is used to calculate the Kolmogorov and Batchelor scales in order to compare with local grid size. Fig. 5 shows the distribution of the Batchelor scale for a representative snapshot of the flow at $Ra = 10^{13}$ with polynomial order 7. It is evident that small element size is needed along the bottom forcing boundary and the right-most 20% of the enclosure. A check of the Batchelor scale against local grid resolution determined that the Batchelor scales are fully resolved in these simulations.

2.2. Convergence and thermal equilibrium

For unsteady flows, meaningful statistics can only be obtained when the flows have reached a thermal equilibrium state. This equilibrium is determined using a time history of the net heat flux through the horizontal base. In horizontal convection, the net heat flux across any horizontal level sum to zero [14,27]. For steady flow, the instantaneous heat flux across the base and any horizontal level will be zero. However, for unsteady flow at thermal equilibrium, the net heat flux fluctuates about a zero mean. In these cases, the discrepancy between the computed time-averaged base heat flux and zero is used to judge for

Fig. 3. A plot showing the nearest 30% of the enclosure to the right-hand (hot) end with clustering toward all wall boundaries to fully resolve small scale structures at high Rayleigh numbers.
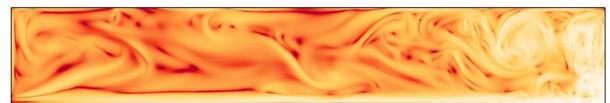

Fig. 5. Contours of the local Batchelor scale (η_b) of the full enclosure with contour level ranges from 2.5×10^{-4} (white) to 0.01 (dark red) for the case of $Ra = 10^{13}$ with a polynomial order of 7. The Batchelor scales are fully resolved.

thermal equilibrium. For the current simulations, this net flux amplitude is well below 2% for $Ra < 10^{12}$ and rises to $< 5\%$ for high Rayleigh number simulations. These deviations are consistent with the experiments of Mullarney et al. [10] and the numerical simulations of Gayen et al. [17].

Three-dimensional direct numerical simulation (DNS) solutions are obtained by way of Fourier expansion in the spanwise direction with a spanwise width of $0.04L$ to be consistent with [17]. To assess the resolution needed in the spanwise direction, simulations incorporating several different spanwise Fourier resolutions were conducted at different Rayleigh numbers. The time averaged kinetic energy in each Fourier mode was computed, with the results plotted in Fig. 6. The modal energy is highest at small wavenumbers, and with increasing wavenumber the modal energy decreases. The trends become approximately linear as the wavenumber increases, which given the log-linear axes reflects an exponential decay in modal energy with increasing spanwise wavenumber. The decay is stronger at smaller Rayleigh numbers, demonstrating the relatively greater influence of thermal and molecular diffusion on flow structures of a given scale compared to higher Rayleigh numbers. Adequate spanwise resolution is determined by a smooth decay of modal energies towards the highest resolved wavenumbers, and a small value of the ratio of energy in the largest resolved wavenumber to the energy in the most energetic wavenumber. For $Ra \leq 10^{11}$, 64 Fourier modes are sufficient to reduce the mean kinetic energy to well below a minuscule $\mathscr{O}(10^{-10})$ (corresponding to a ratio of velocities between in smallest scales and the dominant flow features of order $\mathscr{O}(10^{-5})$). 96 Fourier modes are needed to resolve a similar range of energies for $Ra = 10^{12}$, and 128 modes are needed for $Ra > 10^{12}$.

Table 1 gives the ratio of mean kinetic energy computed for different Rayleigh numbers with different number of Fourier modes in the spanwise direction. It shows that $Ra = 10^{13}$ requires 128 Fourier modes to properly resolve the flow. In this paper, 64 Fourier modes are used for $Ra \leq 10^{12}$, 96 and 128 Fourier modes are used for $Ra = 3.2 \times 10^{12}$ and 10^{13}, respectively.

3. Result and discussion

Numerical experiments were conducted on a rectangular enclosure with an aspect ratio $H/L = 0.16$ and $Pr = 6.14$, with Ra and thermal profile shape parameter n being varied. The temperature differential imposed along the forcing boundary compels the fluid to rise at the more buoyant (hotter) end of the enclosure and descend at the less buoyant (colder) end. The Rayleigh numbers computed in these simulations range from $Ra = 10^3$ to $\mathscr{O}(10^{13})$. In order to reduce computational time, $Ra > 10^{11}$ cases were started from a solution at thermal equilibrium
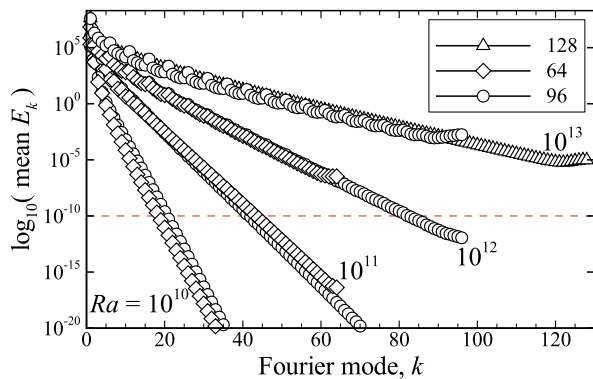

Fig. 6. A comparison of time-averaged kinetic energy in each spanwise Fourier mode for simulations at Rayleigh numbers with spanwise Fourier resolutions as indicated. These simulations had $H/L = 0.16$, $Pr = 6.14$ and $n = 1$.

Table 1
The mean kinetic energy ratio between the highest-wavenumber Fourier mode and the fundamental (most energetic) Fourier mode resolved in each three-dimensional simulation test case, at the stated Rayleigh numbers and resolutions specified.

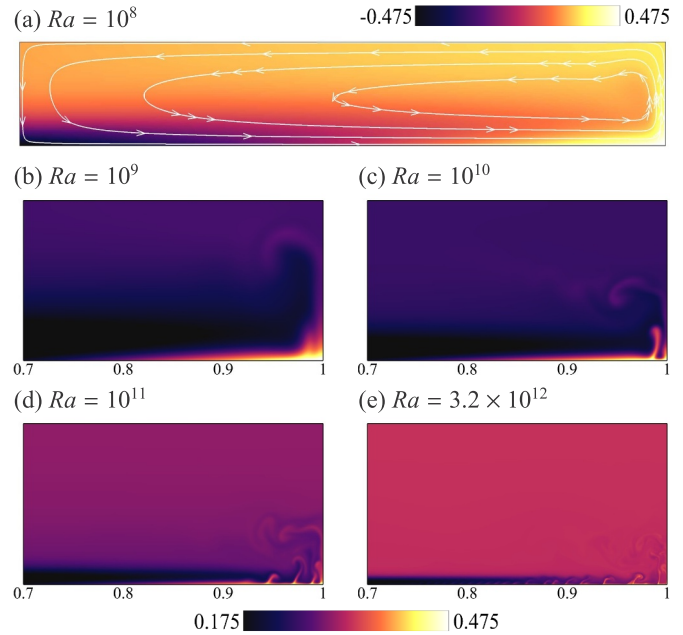| Ra	Number of Fourier modes	$E_{k(m-1)}/E_{k(1)}$
10^{10}	64	8.20×10^{-40}
10^{11}	64	3.31×10^{-21}
10^{12}	64	2.40×10^{-13}
10^{12}	96	4.72×10^{-18}
10^{13}	96	8.70×10^{-10}
10^{13}	128	1.93×10^{-11}

Fig. 7. (a) A plot of temperature contour and streamlines of the full enclosure for $Ra = 10^8$ with contour level ranges from -0.475 (dark shading) to 0.475 (light shading). (b)–(e) Close-up ($0.7L$ toward the hot end of the enclosure) plot of temperature contour at different Rayleigh numbers, Ra for a linear temperature profile, $n = 1$, imposed along the bottom boundary, contour level ranges from 0.175 (dark shading) to 0.475 (light shading) denote cooler and hotter fluid, respectively.
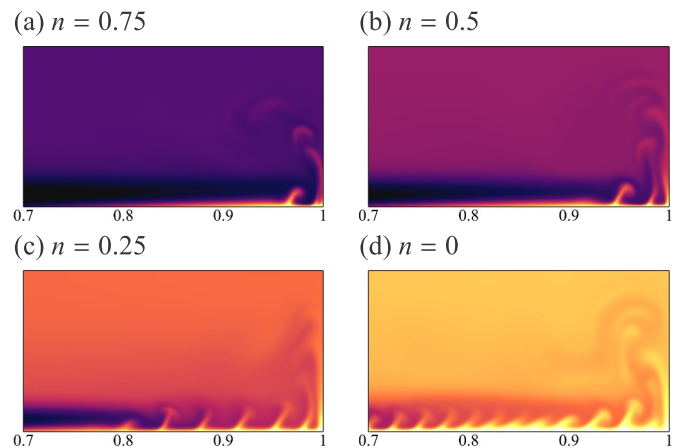

Fig. 8. Close-up ($0.7L$ toward the hot end of the enclosure) plot of temperature contour overlay with streamline for different forcing temperature profile parameter, n with $Ra = 10^{10}$, dark and light shading denote cooler and hotter fluid with the same contour levels as in Fig. 7(b–e).
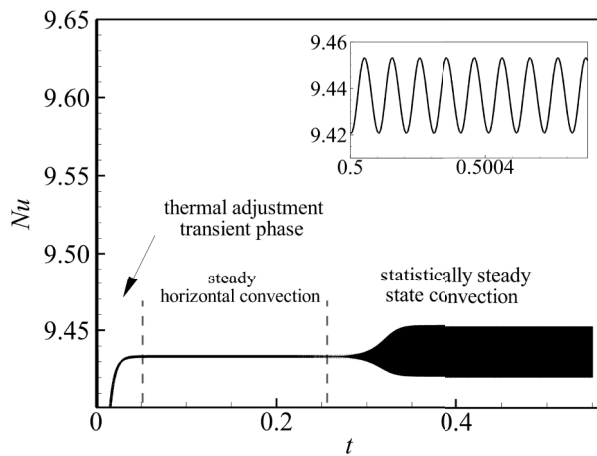
Fig. 9. Temporal evolution of Nusselt number for $Ra = 5.5 \times 10^8$ with a linear thermal forcing along the bottom boundary, showing a temporal adjustment of the Nusselt number from a conduction phase to a convection dominating phase which gives rise to a time periodic regime. Inset: a detail view of the saturated behaviour demonstrating the perfectly time periodic nature of the flow.

computed at a lower Rayleigh numbers. The time step required to maintain numerical stability ranges from 10^{-3} for the lower Rayleigh numbers to 10^{-10} towards the higher end of the Rayleigh number range.

3.1. Two-dimensional flow dynamics

A horizontal temperature gradient imposed along the bottom boundary of the enclosure transfers heat into the enclosure via molecular conduction from the wall to the adjacent fluid. Depending on the strength of thermal forcing, a horizontal thermal boundary layer develops, carrying heat along the bottom boundary leading to a convection-dominated flow within the enclosure. Under a linear ($n = 1$) temperature profile along the bottom boundary in the conduction regime at low Rayleigh numbers, heat transfers through molecular diffusion into the domain creating a symmetric streamline pattern over the whole enclosure. However, this symmetry is broken with a progressive increase in the Rayleigh numbers, as depicted in Fig. 7. At $Ra = 10^8$, a thermal boundary layer is visible along the forcing boundary, transporting colder fluid toward the hotter end. The streamlines began to cluster toward the hot end of the enclosure to form a vertical thermal pathway transporting heat toward the top boundary. As heat travels upward and horizontally along the top boundary toward the colder end of the enclosure thermal energy is lost. This cooling effect eventually brings the fluid down over the cold stable boundary layer along the lower boundary. The end wall jet transports hear convectively into the enclosure to create a mixed conductive-convective regime with very little localised entrainment. In this mixed conduction/convection regime, streamlines are mostly symmetric about the horizontal mid-plane but skewed toward the vertical end wall as shown in Fig. 7(a). This asymmetric convection cell was first suggested by Stommel [13] and later observed experimentally by Rossby [22].

A close-up plot of the temperature contour with a linear temperature profile at different Rayleigh numbers are shown in Fig. 7. The flow changes from a mixed conduction/convection regime (Fig. 7(a)–(c)) to a convection dominated regime (Fig. 7(d) and (e)) at higher Rayleigh numbers. The mixed regime is characterised by the formation of a thermal boundary layer convecting heat along the bottom boundary and a single end wall plume which rises up to the top of the enclosure. The flow dynamics are different when the Rayleigh number is increased beyond 10^{10} into the convection dominated regime, where the thermal boundary layer is becoming thinner. The thermal energy is creating a strong convective forcing which is sufficient for the thermal boundary

layer to erupt from the surface creating multiple thin thermal plume like structures near the end wall. As the single plume is broken up into multiple plumes, with a linear temperature forcing, these thinner plumes do not have sufficient energy to reach the top boundary. Instead, part of the end wall plume convects horizontally near mid-height into the interior, entraining colder fluid along the way over the thermal boundary layer to form a localised circulation confined within the rightmost 10% of the enclosure. Thus, the structure of the flow can be classified into three regimes: a conduction dominated regime, a transitional regime and a convection dominated regime. Within the convection dominated regime, the flow can be further subdivided into a time-independent stable state, a time-periodic state and a time-dependent chaotic state [33], which will be discussed in the following section.

As the temperature profile parameter is changed from a linear ($n = 1$) towards a step ($n = 0$) profile, the horizontal thermal gradient $\partial\theta/\partial x$ increases in the vicinity of the mid-point of the forcing boundary. The higher rate of change of the wall temperature at smaller n in this region leads to higher local vertical temperature differentials in the thermal boundary layer between the cooler fluid convecting in the boundary layer and the increasingly hotter wall. This shifts the locally unstable region [33] further upstream, and promotes the formation of thermal plumes further upstream from the end wall. This can be seen in Fig. 8, where the inception of plume eruptions moves upstream and their frequency increases as the temperature profile parameter is reduced
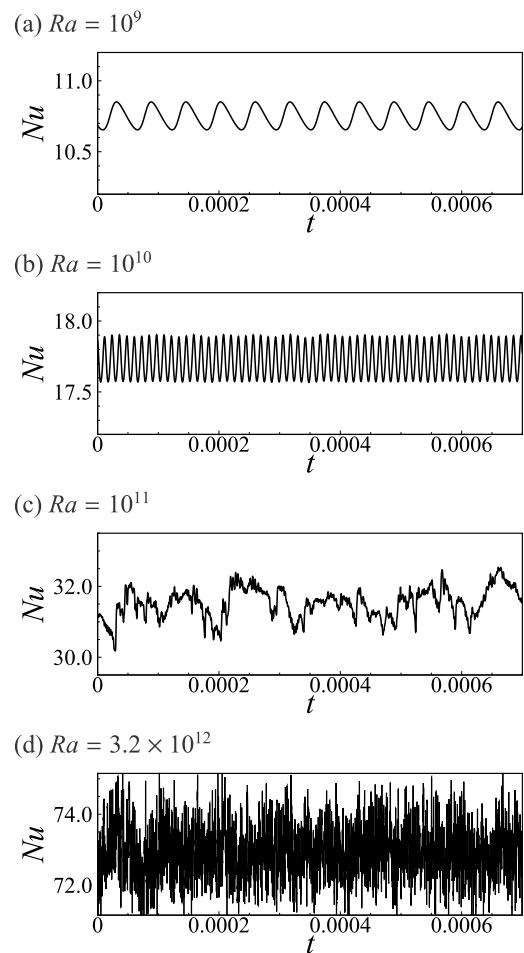

Fig. 10. Time history fluctuation of the Nusselt number for a linear temperature profiles with different Rayleigh numbers. The Rayleigh number ranges from a perfectly time-periodic flow to an aperiodic regime and subsequently transition to a fully unsteady regime. The time $t = 0$ represents an arbitrary time when the simulations had reached a thermal equilibrium and flow statistics were being collected.

toward a step profile ($n = 0$) at a fixed $Ra = 10^{10}$. In addition, the end wall plume penetrates further into the interior altering the stable stratification within the top half of the enclosure. The shape of the temperature profile significantly changes the size of the local circulation zone. This localised region expands upstream to cover roughly 25% of the enclosure (Fig. 8(d)). The circulation also changes from a small, localised behaviour (Fig. 7(c)) to a more global and larger structure as shown in Fig. 8(d). The step profile resembles Rayleigh–Bénard Poiseuille (RBP) flows [36], where the uniformly heated region acts as a Rayleigh–Bénard convection with a horizontal streamwise flow induced by the global overturning circulation. Kelly [36] showed longitudinal rolls (correspond to convection rolls in the streamwise direction) are preferred instability mode over transverse rolls in RBP flows. However, at high Rayleigh number, three-dimensional effects become significant resulted in an interaction between the longitudinal and transverse rolls to form a complex three-dimensional dynamics which are discussed in § 3.6.

3.2. Unsteadiness in horizontal convection

The simulations were carried out over long times to ensure that the flow had reached a thermal equilibrium state before statistics are collected. With the linear temperature forcing along the bottom boundary, a steady state solution without any temporal changes in the Nusselt number is obtained for $Ra < 5.456 \times 10^8$, the maximum changes in the velocity and temperature within the enclosure are of the order 10^{-13} and 10^{-15}, respectively. This shows a high level of convergence for the solution at these Rayleigh numbers. When the Rayleigh number is increased to 5.5×10^8 and beyond the time independent solution is no longer stable; the flow experiences a transition to a perfectly time periodic state as shown in Fig. 9. The figure illustrates a thermal adjustment phase where thermal energy is conductively transferred from the forcing boundary into the interior. This is followed by a region of nearly constant Nusselt number corresponding to steady horizontal convection along the bottom thermal boundary layer, which produces a single end wall plume. Local linear stability analysis [33] and sensitivity analysis [37] reveal a convective two-dimensional instability in the boundary layer, and that beyond $Ra \approx 5.5 \times 10^8$ leads to a time-periodic sustained convection of two-dimensional (transverse-roll structures) within the boundary layer, which are seen in the three-dimensional DNS of Gayen et al. [17] for horizontal convection with a near step-shaped thermal profile. The close-up inset in Fig. 9 depicts the time-periodic nature of the flow at this Rayleigh number.

The perfect periodicity of the flow is maintained up to a Rayleigh number of 10^9 as shown in Fig. 10(a). When the Rayleigh number is increased to 10^{10}, the Nusselt number time history in Fig. 10(b) shows a slight aperiodicity suggestive of a longer-timescale behaviour disrupting the periodic convecting rolls detected at lower Rayleigh numbers. This aperiodic behaviour is attributed to a strong localised re-circulation near the end wall. This can be seen in the thermal field visualisation in Fig. 7 (c), which shows the end wall plume deviating inward at mid-height, creating a stronger local circulation rather than driving the main overturning circulation. The aperiodic separation from the hot end-wall and leftward intrusion of eddies in opposition to the horizontal convection boundary is the source of the aperiodic behaviour detected in Fig. 10(b).

Intermittent noise set in at $Ra = 10^{11}$, which correlates with the eruption of plumes from the bottom boundary in advance of the end wall plumes which enhance local mixing and introduce high frequency noise. These short-wavelength and high-frequency oscillations are superimposed on a longer-wavelength and lower-frequency overturning circulation. With increased Rayleigh number, the thermal boundary layer becomes thinner, and correspondingly the plume structures are smaller and thus more closely spaced (Fig. 7(c and d)). $Ra = 3.2 \times 10^{12}$ shows a continuation of the behaviour observed at $Ra = 10^{11}$, yielding the highly aperiodic Nusselt number time history shown in Fig. 10(d).
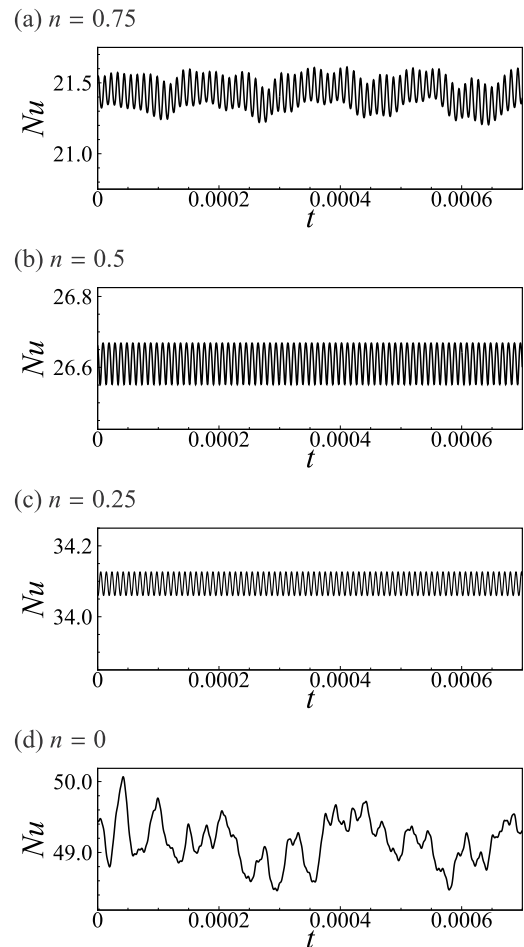

Fig. 11. A plot showing effect of the forcing temperature profile on the Nusselt number fluctuation at $Ra = 10^{10}$. Different ranges are used for the vertical axis to better illustrate individual characteristics of the Nusselt number fluctuation for each of the temperature profile. The Rayleigh number is chosen to match those used in Fig. 8. The time $t = 0$ represents an arbitrary time when the simulations had reached a thermal equilibrium and flow statistics were being collected.

Fig. 11 shows the effect of different forcing temperature profiles on the time history of the Nusselt number at $Ra = 10^{10}$. As the temperature profile changes from a $n = 1$ (linear) to $n = 0.75$, the Nusselt number fluctuation changes from a slightly aperiodic short wavelength oscillation (Fig. 10(b)) to an oscillatory signal with a stronger aperiodicity (Fig. 11(a)). Comparing the thermal fields at $Ra = 10^{10}$ for $n = 1$ (Fig. 7 (b)) and $n = 0.75$ (Fig. 8(a)) demonstrates that in the latter case, the point at which thermal plumes erupt from the boundary layer has advanced upstream, while the end-wall plume continues to intrude above the boundary layer. It is believed that the increased scope for interaction between erupting plumes and the intruding end-wall plume generates the greater aperiodicity detected with $n = 0.75$ over the $n = 1$ profile.

When the temperature profile is adjusted further to $n = 0.5$ (Fig. 11 (b)), the flow returned to a perfectly periodic oscillation in the Nusselt number. Comparing the temperature field between $n = 0.75$ (Fig. 8(a)) to $n = 0.5$ (Fig. 8(b)), while the inception of boundary plume eruptions has advanced further upstream, at $n = 0.5$ the end-wall plume now ascends to the top of the enclosure, which removes the previous interference with the erupting plumes and this explains the recovery of periodicity in this case. At $n = 0.25$, the flow becomes aperiodic with great similarity to the $n = 1$ (linear) case except with a smaller amplitude. The reduction in the amplitude appears to link to an increase in
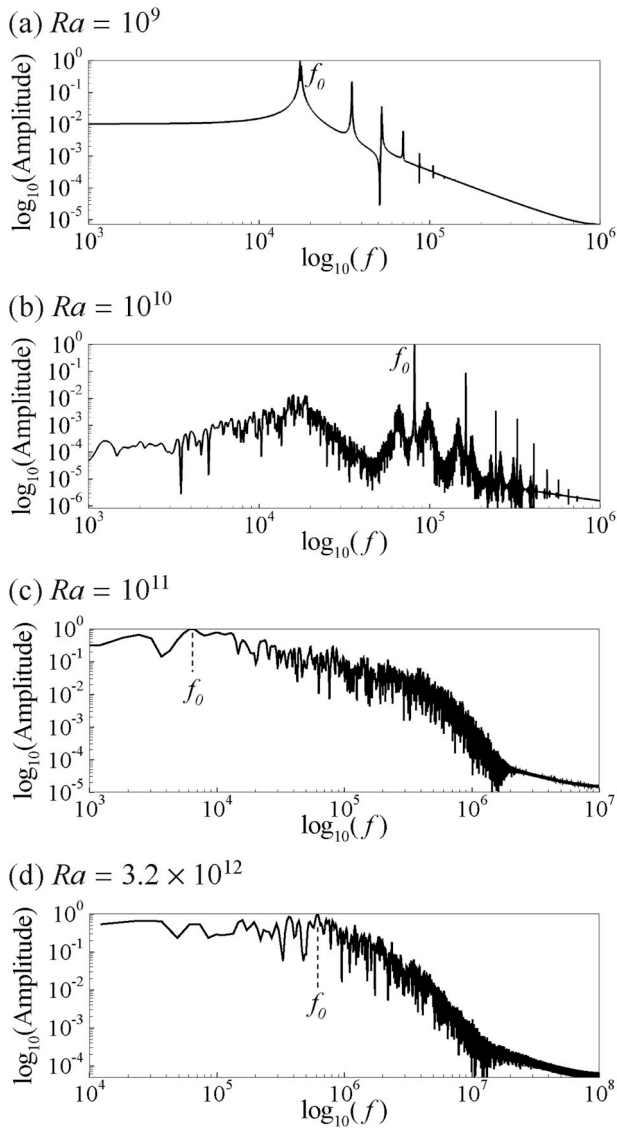
Fig. 12. FFT spectrum of the Nusselt number for a linear temperature profiles with different Rayleigh numbers. The panels show the transition from a periodic to a quasi-periodic and subsequently to an unsteady regime as a function of the Rayleigh number. In each panel the abscissa is linear in frequency and logarithmic in the amplitude.

Fig. 13. FFT spectrum of the Nusselt number at $Ra = 10^{10}$ with different temperature parameters. In each panel the abscissa is linear in frequency and logarithmic in the amplitude.

thermal layer thickness, whereas the aperiodicity most likely comes from the formation of multiple plumes ahead of the end wall. With a step temperature profile, the flow becomes increasingly unsteady as shown in Fig. 11(d).

As the temperature profile changes from a linear profile to a step profile, the thermal boundary layer thickness increases to facilitate a better transport of heat along the end side wall into the domain, creating a stronger overturning circulation. In addition, the number of thermal plumes increases with increasing thermal gradient, which introduce short wavelength and high frequency oscillation locally near the hot end of the enclosure. The relative strength of the overturning circulation and localised unsteady plumes give rise to the variation in Nusselt number fluctuation observed in Fig. 11. Analysis of the Fourier spectra from these cases is contained in the section to follow.

3.3. Flow periodicity

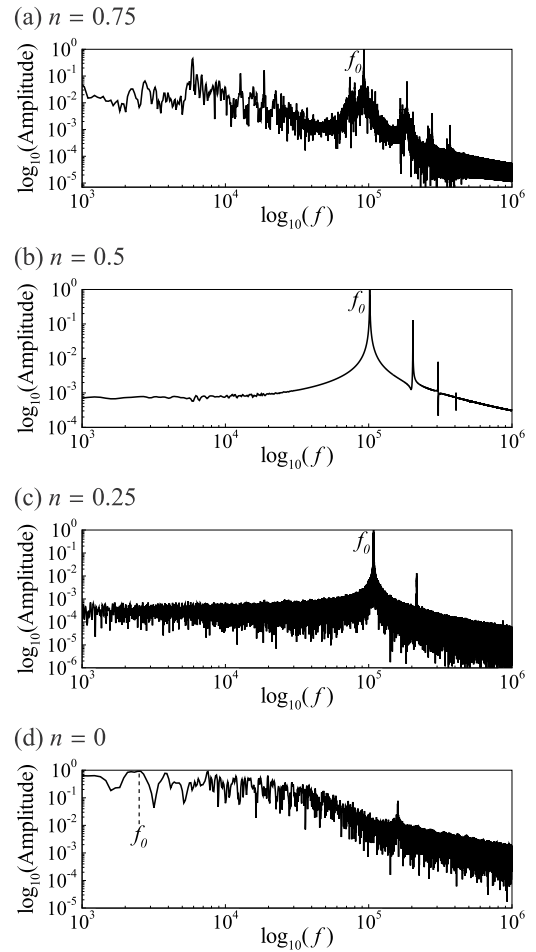Fourier analysis using Fast Fourier Transforms (FFTs) of discrete sampled Nusselt number time history data is used to characterize the periodicity of the flow. The FFT spectrum of the time-periodic Nusselt number fluctuation at $Ra = 10^9$ is shown in Fig. 12(a), indicating a clear dominant fundamental frequency of $f_0 = 1.74 \times 10^4$ along with multiple harmonics which are linear combinations of the fundamental frequency. This is consistent with the time periodic nature of the flow at this Rayleigh number. The flow is weakly convective with an end wall plume transporting heat into the interior creating an overturning circulation, and the fundamental frequency is closely related to the cycle of this circulation. The fundamental frequency increases to $f_0 = 8.16 \times 10^4$ at $Ra = 10^{10}$, where multiple harmonics are clearly visible in the FFT spectrum in Fig. 12(b). The weak aperiodicity in the signal in this case is reflected by the noisier spectrum and a broad low-frequency peak at $f \approx 2 \times 10^4$. At $Ra \geq 10^{11}$ (Fig. 12(c and d)) the FFT spectra exhibit more pronounced broadband noise and significant energy across the low frequencies that occludes the peak associated with the plume eruptions, reflecting the aperiodic flows at these Rayleigh numbers.

The frequency spectral captured at $Ra = 10^{10}$ and different temperature profile parameters are shown in Fig. 13. The spectrum for $n = 0.75$ has a similar structure that of the linear temperature profile, with a clear dominant frequency, visible harmonics, and broadband noise. However, in this case the low frequency noise has a higher amplitude than the $n = 1$ case. Further reduction to $n = 0.5$ results in a spectrum consistent with the perfectly periodic flow with very little noise. Low amplitude noise observed for $n = 0.25$, with a single dominant frequency. The dominant frequency for n value of $0.75, 0.5$ and 0.25 are $f_0 = 9.26 \times 10^4, 1.02 \times 10^5$ and 1.08×10^5, respectively, which are slightly higher than the $n =$

1 at the same Rayleigh number. As expected, with $n = 0$, the flow becomes unsteady and non-periodic as shown in Fig. 13(d).

3.4. Onset of time-dependent flow

The Stuart–Landau model is a useful mathematical tool to understand a complex flow phenomenon. It is used to investigate the nature and behaviour of flow in the vicinity of a transition from steady to time-periodic state. This analysis had been used extensively to study the transition of different wake modes behind bluff bodies [38–41]. A brief overview of its application in the current study is provided here.

Landau and Lifshitz [42] proposed a model to describe the growth and saturation of a perturbation near a transition point. The equation of this model can be written as

$$\frac{dA}{dt} = (\sigma + i\omega)A - l(1 + ic)|A|^2 A + \dots, \tag{12}$$

where A is a complex variable representing the fluctuation amplitude of a parameter, σ is the linear growth rate of a perturbation and ω is the angular oscillation frequency during the linear growth phase. A detailed description of this equation is provided in Ref. [38]. Higher-order terms are truncated from the right hand side of the equation. The complex amplitude is considered to take the form

$$A(t) = \gamma(t)e^{i\varphi(t)}, \tag{13}$$

where $\gamma = |A|$ is the real and non-negative amplitude of A, and φ is its phase. Substituting Eq. (13) into the Stuart–Landau equation (Eq. (12)) and separating into real and imaginary parts gives

$$\frac{d\log(\gamma)}{dt} = \sigma - l\gamma^2 + \dots, \tag{14}$$

$$\frac{d(\varphi)}{dt} = \omega - lc\gamma^2 + \dots. \tag{15}$$

where l and c are constants determining the amplitude and frequency of the mode at saturation. From equation (13), a plot of $d\log|A|/dt$ against $|A|^2$ will provide the linear growth rate of instability at $|A|^2 = 0$ and the gradient will determine the non-linear characteristics of the evolving instability. A positive gradient ($-l$) indicates a subcritical bifurcation, whereas a negative gradient ($+l$) indicates a supercritical bifurcation. A subcritical bifurcation permits bi-stability, or hysteresis, in the vicinity of the transition, whereas a supercritical bifurcation is non-hysteretic.

The amplitude of the time-periodic fluctuation of the Nusselt number is used as a measure of the amplitude of the instability leading to time-periodic flow in horizontal convection ($|A|$). To achieve the cleanest possible representation of the instability towards the linear (infinitesimal amplitude) regime, the Landau modelling is performed "in reverse": a time-periodic solution at $Ra = 5.5 \times 10^8$ serves as an initial condition, with simulations impulsively stepped down in Rayleigh number to record $|A(t)|$ as the flow decays to a steady state. Fig. 14(a) shows such a fluctuation when the solution for $Ra = 5.4 \times 10^8$ evolve from $Ra = 5.5 \times 10^8$. Fig. 14(b) shows a plot of ($d\log|A|/dt$) against $|A|^2$, the intersection at $|A|^2 = 0$ gives decay rate of $\sigma = -1.12 \times 10^2$ and the negative slope of the curve demonstrates that the instability occurs through a supercritical bifurcation.

This process was repeated for a number of Rayleigh numbers close to the transitional Rayleigh number, the corresponding global decay rate for each Rayleigh number considered is shown in Fig. 14(c). Linear extrapolation of these data to zero growth refines our estimate of the critical Rayleigh number to $Ra = 5.46 \times 10^8$. Paparella and Young [14] had put the transition Rayleigh number at 3×10^6 for an enclosure with thermal forcing at its centre, with an aspect ratio of $H/L = 0.25$, and $Pr = 1$. However, to the authors' knowledge this is the first time that the supercritical nature of unsteady flow transition in horizontal convection has been demonstrated.

The critical Rayleigh number for different temperature profiles were found using this same method, with results shown in the second column of Table 2. There is a downward trend in the critical Rayleigh number as the profile is altered from a linear towards a step profile. This likely follows the destabilising behaviour described in Section 3.1, where the steeper thermal gradient at smaller n in the middle region of the base creates strongly unstable gradients in the thermal boundary layer, leading to an advance of instability.

To verify the results of the Stuart–Landau analysis, a range of Rayleigh numbers were computed in a sweep across the transitional regime to confirm both the critical Rayleigh number and the absence of hysteresis based on the fluctuation of the Nusselt number. For the linear temperature profile, the flow changes from a steady state at Rayleigh number of 5×10^8 to a time-periodic state at a Rayleigh number of $5.5 \times$
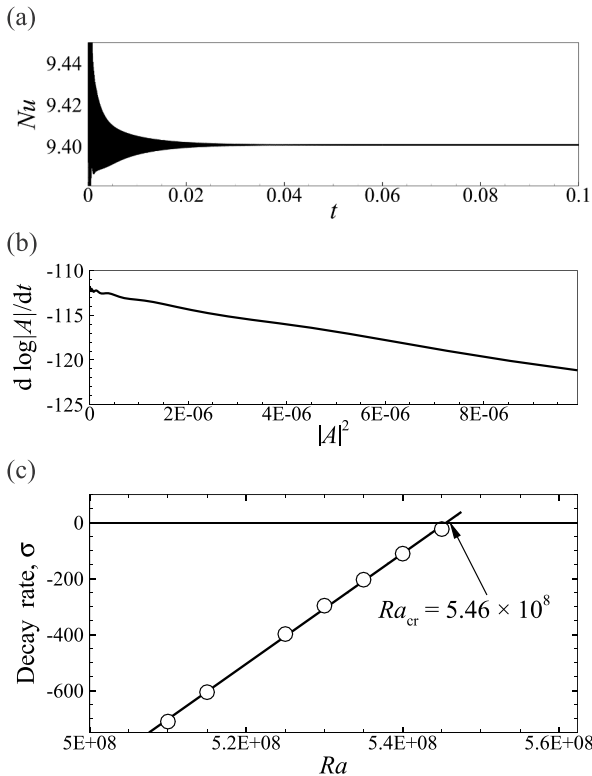
(a)

(b)

(c)

Fig. 14. (a) Temporal evolution of Nusselt number for $Ra = 5.4 \times 10^8$ evolved from a higher periodic Rayleigh number of 5.5×10^8 with a linear temperature profile along the bottom boundary. (b) A plot of $d\log|A|/dt$ against A^2, where A represents the amplitude of the envelope of the Nusselt number. (c) Instability decay rate is plotted against Ra with linear extrapolation to estimate the critical Rayleigh number of the flow.

Table 2
Critical Rayleigh number, Ra_{cr}, determined from the Stuart–Landau analysis as well as with the amplitude fluctuation of the Nusselt number for different temperature parameters.

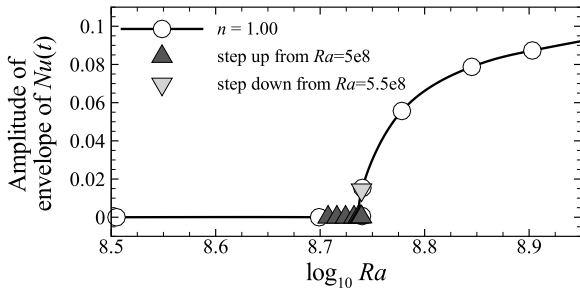| n	Ra_{cr}	
	Landau	Nusselt amplitude
1	5.46×10^8	5.45×10^8
0.75	4.46×10^8	4.50×10^8
0.5	3.06×10^8	3.08×10^8
0.25	1.35×10^8	1.38×10^8
0	8.00×10^7	7.93×10^7

Fig. 15. A time series fluctuation of the Nusselt number along the thermal forcing boundary against $log_{10}Ra$ for the linear temperature profile with refinement of Rayleigh number near the transition Rayleigh number of $Ra = 5.5 \times 10^8$. The $\triangle$ symbols represent refinement started from an initial steady state at $Ra = 5 \times 10^8$ and the ∇ symbol started from the periodic solution at $Ra = 5.5 \times 10^8$.
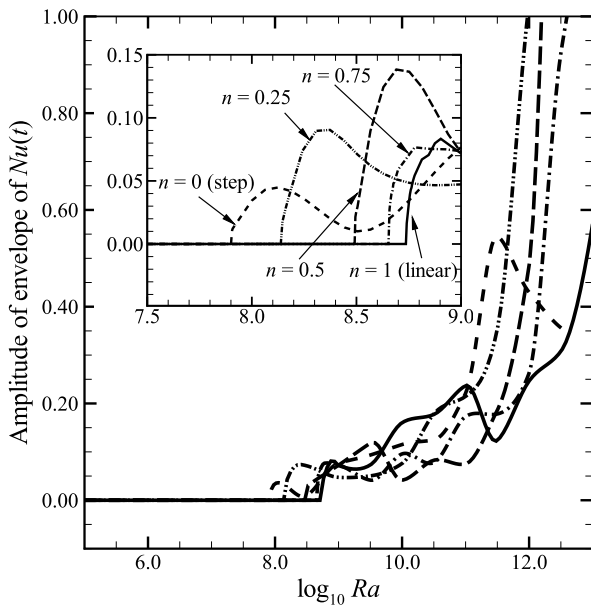

Fig. 16. Figure showing amplitude fluctuation of the Nusselt number against $log_{10}Ra$ for different forcing temperature profile. A close-up of the transitional region is included.

10^8. To pin point the transition Rayleigh number, the steady solution at $Ra = 5 \times 10^8$ was used to evolve flows at higher Rayleigh numbers with an increment of 0.25×10^8.

The resulting amplitudes are shown in Fig. 15, where the nominal flow transitions is at $Ra = 5.45 \times 10^8$. Using this method, the critical Rayleigh numbers for the other temperature profiles are shown in Table 2. The table shows a strong agreement between critical Rayleigh number predicted from the Stuart–Landau analysis and those obtained from the Nusselt number fluctuation.

To test for hysteresis, simulations were run by stepping down the Rayleigh number using an initially unsteady solution from an incrementally higher Rayleigh number. The results from these runs are also shown in Fig. 15. No hysteresis is observed, confirming the Stuart–Landau model prediction of a supercritical bifurcation. The transitional Rayleigh number for the different temperature profiles are revealed in Fig. 16. The plot also includes amplitudes recorded at higher Rayleigh numbers; all temperature profiles developed an aperiodic regime beyond the periodic regime, consistent with the linear profile. The inset in the figure shows that the transitional Rayleigh number
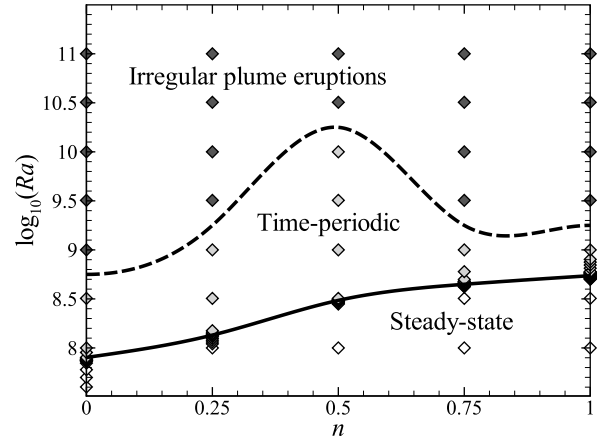

Fig. 17. Flow regimes in the Ra–n parameter space. An unbroken curve marks the threshold between steady-state and time-periodic flow regimes; this threshold has been accurately determined using growth rates obtained from a Stuart–Landau analysis of the time-dependency of the flow. A dashed curve is included for guidance to delineate the time-periodic and irregular plume eruption regimes at higher Rayleigh numbers. Symbols show the parameter combinations that were computed to map this parameter space.

decreases as the temperature profile is changed from a linear to a step function as expected.

The aforementioned results permit the construction of a regime diagram across the Ra–n parameter space, which is plotted in Fig. 17. The plot demonstrates that as the temperature gradient departs from the linear profile towards a step profile, the onset of periodic/chaotic flows occur at a lower Rayleigh number. However, at intermediate profile shapes ($n \approx 0.5$), the transition from periodic to irregular flow is delayed, leading to a wider range of Rayleigh numbers over which time-periodic flow is obtained.

3.5. Heat transfer and scaling at high Rayleigh number

In the case of time-periodic and time-dependent simulations, a statistical mean Nusselt number is obtained from the time series data. Fig. 18(a) plots Nusselt number against Rayleigh number for each of the considered base temperature profiles. Immediately apparent is that at any given Rayleigh number, the linear temperature profile produces the smallest Nusselt numbers, with a monotonic increase in Nusselt number occurring as the profile shifts to a step profile. Convective flow establishes by $Ra = \mathcal{O}(10^7)$ to $\mathcal{O}(10^8)$ from the step profile to the linear profile. A brief region occupying between one and two orders of Rayleigh number exhibit Nusselt numbers that appear to scale with Rayleigh number to the 1/5 th power. A 1/5 th scaling exponent was derived and demonstrated by Rossby [22], and has subsequently been confirmed both experimentally [10] and numerically [17,24].

However, across the investigated range of base temperature profile shapes, the Nusselt numbers can be seen to exhibit an elevation in their scaling at higher Rayleigh numbers. For visual guidance, two dashed lines extrapolating $Nu \sim Ra^{1/5}$ scaling and two dash-dotted lines extrapolating $Nu \sim Ra^{1/4}$ scaling projecting from $Ra = 10^{10}$ for the linear and step temperature profiles are included in Fig. 18(a). The scaling is seen to exceed the 1/5 scaling beyond $Ra = \mathcal{O}(10^8)$ to $\mathcal{O}(10^{10})$. For the subsequent at least four decades in Rayleigh number, the Nusselt number scales close to a 1/4 power of Rayleigh numbers for the linear temperature profile, whereas a less-pronounced increase in the scaling exponent is found as the temperature profile shifts towards a step profile.

Fig. 18(b) plots Nusselt number compensated by $Ra^{1/4}$ against Ra to demonstrate this scaling variation more clearly. The Nusselt numbers
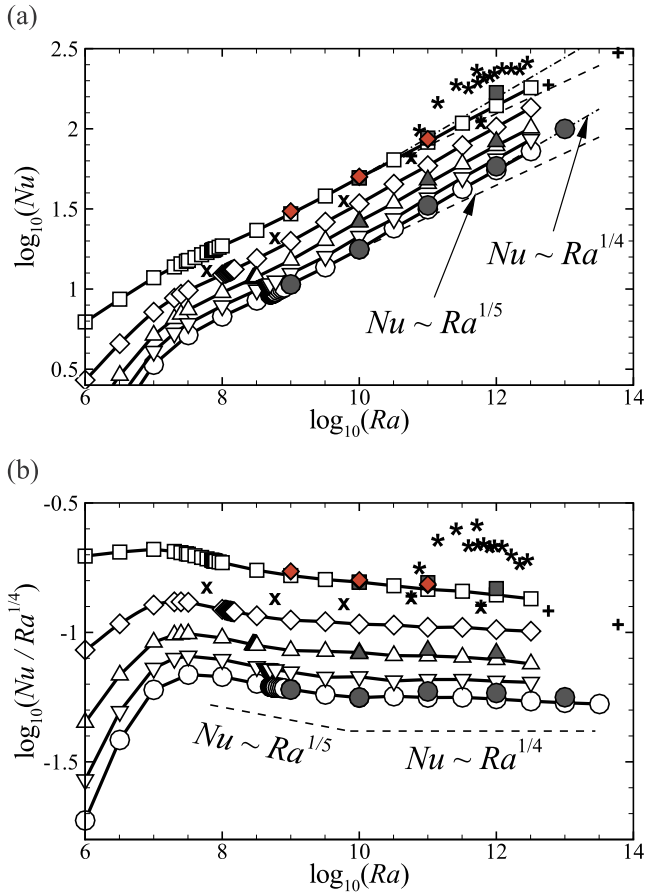
(a)

(b)

Fig. 18. (a) A plot of Nusselt number, *Nu*, against Rayleigh number, *Ra*, with a base 10 logarithmic scale for different temperature forcing profiles. Dashed guidance lines representing $Ra^{1/5}$ scaling extending from $Ra = 10^{10}$ for the temperature profiles of $n = 1$ and 0 are included as a visual guide for assessing the trending gradient along each of the curves. (b) A plot of compensated Nusselt number ($Nu/Ra^{1/4}$) against Rayleigh number, *Ra*, for different temperature profiles, a dashed line representing $Nu \sim Ra^{1/5}$ and a dashed horizontal line representing $Nu \sim Ra^{1/4}$ are included for visual guidance. Symbols $\circ$, $\triangledown$, $\triangle$, $\diamond$, $\square$ represent $n = 1, 0.75, 0.5, 0.25$ and 0, respectively. The filled symbols represent Nusselt number obtained from three-dimensional simulations and the red-filled $\diamond$ are DNS simulations from Shishkina [43]. Symbols $\times$, $+$ and $*$ respectively represent Gayen et al. [17]'s DNS and LES simulations, and Mullarney et al. [10]'s experimental data for comparison.

reported by Ref. [17] are included for comparison, and can be seen to reside between the $n = 0$ and 0.25 data, consistent with their adoption of a slightly smoothed step profile for temperature and the Prandtl number ($Pr = 5$). A possible explanation for the present results is that the linear profile produces horizontal convection flow features that are compatible with one of [27] $Nu \sim Ra^{1/4}$ regimes (I_l^*, III_∞ or IV_u), while towards the step profile the data may reflect the absence of a pure power law: instead exhibiting a behaviour consistent with a linear combination of Rossby's 1/5 th scaling and a $Ra^{1/4}$ scaling regime (analogous to the demonstration by Ref. [28] that a combination of 1/4 and 1/3 power laws in Rayleigh–Bénard convection mimics a 2/7 scaling).

To investigate further, dissipation contributions from the boundary layer and the bulk are extracted for the linear and step temperature profile cases, with the results plotted in Fig. 19. Kinetic and thermal boundary layers thicknesses are defined using the slope-method [4,44] whereby the thickness is taken as the distance between the boundary and the point at which a line tangent to the time-averaged thermal or velocity profile reaches the value of the respective field at its first turning point (the edge of the boundary layer). These thicknesses were
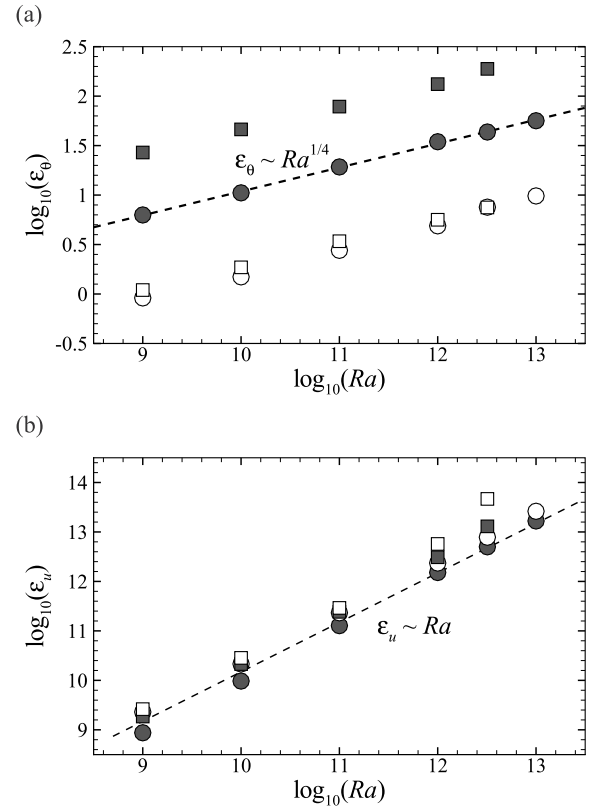

(a)

(b)

Fig. 19. Plots of global time-averaged (a) thermal and (b) kinetic dissipation contributions from the boundary layer (shaded symbols) and the bulk (open symbols). Symbols $\circ$ and $\square$ represent the step and the linear temperature forcing profiles, respectively.

(a) $Ra = 10^{10}$

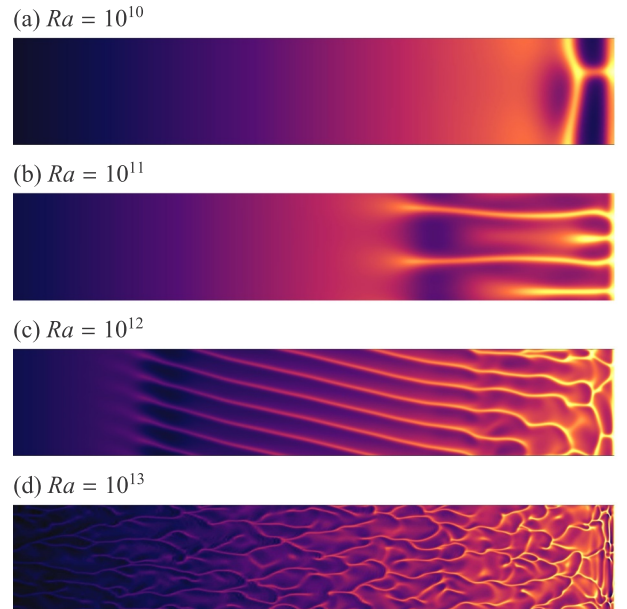(b) $Ra = 10^{11}$

(c) $Ra = 10^{12}$

(d) $Ra = 10^{13}$

Fig. 20. Temperature contours on a horizontal plane at a height 25% of the thermal boundary layer thickness for each of the Rayleigh number used. These cases depict horizontal convection with a linear ($n = 1$) temperature profile at Rayleigh numbers as indicated. The temperature contour levels vary from dark (cold) to light (hot) shading over the range $0.15 \leq \theta \leq 0.475$. The panels show $0.6L$ toward the hot end of the enclosure. Local bright regions reveal regions where heat is convected vertically from nearer to the bottom boundary in plume filaments.

used to calculate dissipation contributions for the boundary layer and the bulk. The thermal dissipation for the linear and step temperature profiles are dominant within the boundary layer for all Rayleigh numbers, as shown in Fig. 19(a). The kinetic dissipation is seen in Fig. 19 (b) to exhibit a similar contribution from the boundary layer and the bulk, which is outside the scope of the theory of Shishkina et al. [27].

It can therefore be concluded that the present data is consistent with the flows exhibiting Rossby's $Nu \sim Ra^{1/5}$ regime and then a zone exhibiting an elevation to $Nu \sim Ra^{1/4}$ as predicted by Shishkina et al.'s [27] theoretical model based on the Grossmann and Lohse's [28] ideas, as applied to horizontal convection. The $Nu \sim Ra^{1/4}$ zone is more prevalent under the linear temperature profile, while the $Ra^{1/5}$ regime being more persistent under the step temperature profile.

3.6. Three-dimensional effects

It has previously been shown [17] that horizontal convection progresses with increased Rayleigh number from a steady-state convective state, through a two-dimensional unsteady state, an ordered three-dimensional state featuring longitudinal-roll structures in the boundary layer, to a disordered state featuring irregular plume filaments erupting from the heated portion of the boundary. Here three-dimensional simulations are conducted to elucidate the development of three-dimensionality across the family of temperature profiles considered in this study. For a linear temperature profile, the flow is found to transition from a steady transverse rolls to a single longitudinal roll at $Ra \approx 10^{10}$, as shown in the temperature field plotted in Fig. 20(a). The figure shows the temperature field on a horizontal plane at height $y = 2 \times 10^{-3}$ which lies within the thermal boundary layer along the bottom wall. This initial behaviour of transverse roll instability paving the way for subsequent longitudinal roll instability was predicted by the linear stability analysis of Tsai et al. [33] for horizontal convection with a linear thermal profile, and is consistent with the three-dimensional DNS for the step profile reported by Gayen et al. [17]. [33] demonstrated that the instability is thermally driven and resembles Rayleigh–Bénard convection with through-flow. Multiple longitudinal rolls are found to develop at a higher Rayleigh number (Fig. 20(b)); this is analogous to multiple cellular structures in Rayleigh–Bénard convection, and is consistent with the spanwise wavelength of the structures scaling with the reducing boundary layer thickness with increased Rayleigh numbers. At $Ra = 10^{11}$, the majority of the thermal energy is carried by the end wall plume into the interior, thus maintaining the longitudinal structures of the flow. However, by $Ra = 10^{12}$ the thermal boundary layer begins to break off into filament plumes channelling heat directly into the interior upstream of the end wall. The enhancement of heat transfer into the interior breaks up the longitudinal rolls into multi-cellular three-dimensional structures occupying approximately the rightmost 10% of the enclosure. The interaction of these plumes with the longitudinal roll structures results in the formation of oblique rolls as observed in the region $0.7L \lesssim x \lesssim 0.9L$ in Fig. 20(c). As more plumes are formed further away from the end wall at $Ra = 10^{13}$, the majority of the transverse and longitudinal rolls give way to irregular thermal plume formation.

The same transitional processes are observed for different imposed temperature profiles, but at a lower Rayleigh number, as the temperature profile varies from a linear to a step profile. Fig. 21 shows the temperature fields on a horizontal plane located within the thermal boundary layer at $Ra = 10^{12}$ over the range of base temperature profiles. For $Ra = 10^{12}$ with a temperature profile $n = 0.5$, the regular oblique roll structures branched out into irregular network of plume lines as shown in Fig. 21(b). Fig. 21(c) shows the temperature field for the same Rayleigh number with a step temperature profile, the lighter colour of the contour indicates a higher interior temperature. Fig. 21 demonstrates that the progression from a linear to a step thermal profile leads to a significant broadening of the region of spatio-temporally chaotic

(a) $Ra = 10^{12}$, $n = 1$ (linear)
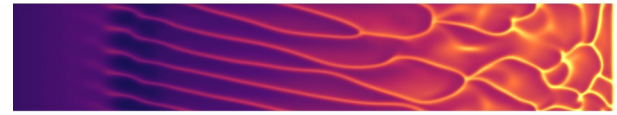
(b) $Ra = 10^{12}$, $n = 0.5$
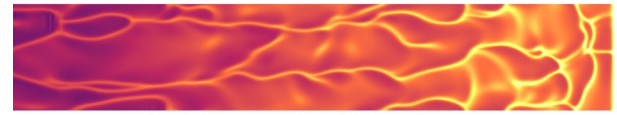
(c) $Ra = 10^{12}$, $n = 0$ (step)

Fig. 21. Temperature on a horizontal plane at a height $y = 2 \times 10^{-3}$ for $Ra = 10^{12}$ with different temperature profiles. The contour levels are the same as Fig. 20.

plume eruptions from approximately the rightmost 10% of the enclosure with $n = 1$ to beyond the depicted 60% at $n = 0.5$ and 0. The spatio-temporal plumes are high dimensional [45], and maintains a relatively simple vertical structure with irregular patterns in time and in the horizontal plane [46].

The compensated Nusselt number ($Nu/Ra^{1/4}$) is computed for three-dimensional simulations, these are plotted in Fig. 18(b) to compare with the two-dimensional simulations. The 3D Nusselt numbers agree well with the two-dimensional simulations, reinforcing the zone of higher $Ra^{1/4}$ scaling behaviour at high Rayleigh number discussed in § 3.5.

4. Conclusions

Horizontal convection at a Prandtl number $Pr = 6.14$ consistent with water is investigated under a systematic variation in the forcing temperature profile imposed along a horizontal boundary using high-resolution spectral element simulations. The flow dynamics, stability, time-dependency and heat transfer behaviours are presented. It is confirmed that for all forcing profiles considered, at sufficiently high Rayleigh numbers, heat transfer is dominated by convection where plume-like structures break out of the thermal boundary layer, establishing a time periodic instability within the system. The periodic regime quickly gives way to a chaotic behaviour with further increases in Rayleigh number. A Stuart–Landau analysis reveals that transition from steady to time-periodic convection is found to occur through a supercritical (non-hysteretic) bifurcation across all imposed temperature profiles, with the step profile being the most unstable; the critical Rayleigh number increases monotonically from $Ra_c \approx 8.0 \times 10^7$ to 5.5×10^8 between the step and linear profiles, respectively. These critical Rayleigh numbers were confirmed using a sweeping method.

Shortly after the inception of convective flow, an upward trend in the scaling exponent was obtained at higher Rayleigh numbers, adopting a value moderately in excess of $1/5$ for a step temperature profile, with a progressively larger range of higher Rayleigh numbers exhibiting an uplift to a behaviour consistent with $Nu \sim Ra^{1/4}$ for profiles approaching a linear temperature variation. This findings corroborates recent theoretical scaling predictions of Shishkina et al. [27,43], and extends the range of Rayleigh numbers over which the $Ra^{1/4}$ scaling regime has been found to $Ra = 3.2 \times 10^{13}$, up from $Ra = 2 \times 10^{11}$.

This research highlights the importance of the horizontal buoyancy forcing profile in determining the scaling and stability of horizontal convection at a given Rayleigh number, the robustness of the scalings across different temperature forcings, and additionally illustrates the consistency between scalings captured by two-dimensional simulations

and three-dimensional DNS.

Acknowledgements

References

[1] G.A. Glatzmaier, R.S. Coe, L. Hongre, P.H. Roberts, The role of the Earth's mantle in controlling the frequency of geomagnetic reversals, Nature 401 (1999) 885–890.

[2] J. Marshall, F. Schott, Open-ocean convection: observations, theory, and models, Rev. Geophys. 37 (1999) 1–64.

[3] F. Pigeonneau, J.-M. Flesselles, Practical laws for natural convection of viscous fluids heated from above in a shallow cavity, Int. J. Heat Mass Transf. 55 (2012) 436–442.

[4] G. Ahlers, S. Grossmann, D. Lohse, Heat transfer and large scale dynamics in turbulent Rayleigh-Bénard convection, Rev. Mod. Phys. 81 (2009) 503.

[5] L.P. Kadanoff, Turbulent heat flow: structures and scaling, Phys. Today 54 (2001) 34–39.

[6] F. Chillò, J. Schumacher, New perspectives in turbulent Rayleigh-Bénard convection, Eur. Phys. J. E (EPJ E), - Soft Matter 35 (2012) 1–25.

[7] H. Bénard, Les tourbillons cellulaires dans une nappe liquide propageant de la chaleur par convection: en régime permanent, Gauthier-Villars, 1901.

[8] L. Rayleigh, Lix. on convection currents in a horizontal layer of fluid, when the higher temperature is on the under side, the London, Edinburgh, and Dublin, Philos. Mag. J. Sci. 32 (1916) 529–546.

[9] M.E. Stern, Ocean Circulation Physics, ume 246, Academic Press, New York, 1975.

[10] J.C. Mullarney, R.W. Griffiths, G.O. Hughes, Convection driven by differential heating at a horizontal boundary, J. Fluid Mech. 516 (2004) 181–209.

[11] G.O. Hughes, R.W. Griffiths, Horizontal convection, Annu. Rev. Fluid Mech. 40 (2008) 185–208.

[12] B.A. Warren, Deep circulation of the world ocean, in: B.A. Warran, C. Wunsch (Eds.), Evolution of Physical Oceanography, Scientific Surveys in Honor of Henry Stommel, The MIT Press, Cambridge, Massachusetts, 1981, pp. 6–41.

[13] H. Stommel, On the smallness of sinking regions in the ocean, Proc. Natl. Acad. Sci. U.S.A. 48 (1962) 766.

[14] F. Paparella, W.R. Young, Horizontal convection is non-turbulent, J. Fluid Mech. 466 (2002) 205–214.

[15] S. Chiu-Webster, E.J. Hinch, J.R. Lister, Very viscous horizontal convection, J. Fluid Mech. 611 (2008) 395–426.

[16] W. Wang, R.X. Huang, An experimental study on thermal circulation driven by horizontal differential heating, J. Fluid Mech. 540 (2005) 49–73.

[17] B. Gayen, R.W. Griffiths, G.O. Hughes, Stability transitions and turbulence in horizontal convection, J. Fluid Mech. 751 (2014) 698–724.

[18] E. Bilgen, R.B. Yedder, Natural convection in enclosure with heating and cooling by sinusoidal temperature profiles on one side, Int. J. Heat Mass Transf. 50 (2007) 139–150.

[19] P. Khansila, S. Witayangkurn, Visualization of natural convection in enclosure filled with porous medium by sinusoidally temperature on the one side, Appl. Math. Sci. 6 (2012) 4801–4812.

[20] R.W. Griffiths, B. Gayen, Turbulent convection insights from small-scale thermal forcing with zero net heat flux at a horizontal boundary, Phys. Rev. Lett. 115 (2015) 204301.

[21] R. Barkan, K.B. Winters, S.G.L. Smith, Rotating horizontal convection, J. Fluid Mech. 723 (2013) 556–586.

[22] H.T. Rossby, On thermal convection driven by non-uniform heating from below: an experimental study, Deep Sea Res. Oceanogr. Abstr. 12 (1965) 9–16.

[23] J.H. Siggers, R.R. Kerswell, N.J. Balmforth, Bounds on horizontal convection, J. Fluid Mech. 517 (2004) 55–70.

[24] G.J. Sheard, M.P. King, Horizontal convection: effect of aspect ratio on Rayleigh number scaling and stability, Appl. Math. Model. 35 (2011) 1647–1655.

[25] M. Ilıcak, G.K. Vallis, Simulations and scaling of horizontal convection, Tellus A 64 (2012) 18377.

[26] M.A. Coman, R.W. Griffiths, G.O. Hughes, The sensitivity of convection from a horizontal boundary to the distribution of heating, J. Fluid Mech. 647 (2010) 71.

[27] O. Shishkina, S. Grossmann, D. Lohse, Heat and momentum transport scalings in horizontal convection, Geophys. Res. Lett. 43 (2016) 1219–1225.

[28] S. Grossmann, D. Lohse, Scaling in thermal convection: a unifying theory, J. Fluid Mech. 407 (2000) 27–56.

[29] M.G. Rosevear, B. Gayen, R.W. Griffiths, Turbulent horizontal convection under spatially periodic forcing: a regime governed by interior inertia, J. Fluid Mech. 831 (2017) 491–523.

[30] P. Hignett, A. Ibbetson, P.D. Killworth, On rotating thermal convection driven by non-uniform heating from below, J. Fluid Mech. 109 (1981) 161–187.

[31] W.K. Hussam, T.K. Tsai, G.J. Sheard, The effect of rotation on radial horizontal convection and Nusselt number scaling in a cylindrical container, Int. J. Heat Mass Transf. 77 (2014) 46–59.

[32] G.J. Sheard, W.K. Hussam, T. Tsai, Linear stability and energetics of rotating radial horizontal convection, J. Fluid Mech. 795 (2016) 1–35.

[33] T. Tsai, W.K. Hussam, A. Fouras, G.J. Sheard, The origin of instability in enclosed horizontally driven convection, Int. J. Heat Mass Transf. 94 (2016) 509–515.

[34] O. Shishkina, R.J.A.M. Stevens, S. Grossmann, D. Lohse, Boundary layer structure in turbulent thermal convection and its consequences for the required numerical resolution, New J. Phys. 12 (2010), 075022.

[35] G. Grötzbach, Revisiting the resolution requirements for turbulence simulations in nuclear heat transfer, Nucl. Eng. Des. 241 (2011) 4379–4390.

[36] R. Kelly, The onset and development of thermal convection in fully developed shear flows, in: Advances in Applied Mechanics, ume 31, Elsevie, 1994, pp. 35–112.

[37] M.A. Leigh, T. Tsai, G.J. Sheard, Probing horizontal convection instability via perturbation of the forcing boundary layer using a synthetic jet, Int. J. Therm. Sci. 110 (2016) 251–260.

[38] M. Provansal, C. Mathis, L. Boyer, Bénard-von Kármán instability: transient and forced regimes, J. Fluid Mech. 182 (1987) 1–22.

[39] P. Le Gal, A. Nadim, M. Thompson, Hysteresis in the forced Stuart–Landau equation: application to vortex shedding from an oscillating cylinder, J. Fluids Struct. 15 (2001) 445–457.

[40] G.J. Sheard, M.C. Thompson, K. Hourigan, Asymmetric structure and non-linear transition behaviour of the wakes of toroidal bodies, Eur. J. Mech. B Fluid 23 (2004) 167–179.

[41] G.J. Sheard, M.C. Thompson, K. Hourigan, From spheres to circular cylinders: non-axisymmetric transitions in the flow past rings, J. Fluid Mech. 506 (2004) 45–78.

[42] L.D. Landau, E.M. Lifshitz, Mechanics, third ed., Pergamon, 1976.

[43] O. Shishkina, Mean flow structure in horizontal convection, J. Fluid Mech. 812 (2017) 525–540.

[44] J.D. Scheel, J. Schumacher, Local boundary layer scales in turbulent Rayleigh–Bénard convection, J. Fluid Mech. 758 (2014) 344–373.

[45] G. Ahlers, Experiments on spatio-temporal chaos, Phys. A Stat. Mech. Appl. 249 (1998) 18–26.

[46] E. Bodenschatz, W. Pesch, G. Ahlers, Recent developments in Rayleigh–Bénard convection, Annu. Rev. Fluid Mech. 32 (2000) 709–778.